JOURNAL OF COMPUTATIONAL PHYSICS **126,** 373–389 (1996)
ARTICLE NO. 0144

The Effects of Numerical Viscosities

I. Slowly Moving Shocks

SHI JIN*,[1] AND JIAN-GUO LIU†,[2]

*School of Mathematics, Georgia Institute of Technology, Atlanta, Georgia 30332 and †Department of Mathematics, Temple University, Philadelphia, Pennsylvania 19122

Received June 19, 1995; revised November 6, 1995

We begin a systematical study on the effect of numerical viscosities. In this paper we investigate the behavior of shock-capturing methods for slowly moving shocks. It is known that for slowly moving shocks even a first-order scheme, such as the Godunov or Roe type methods, will generate downstream oscillatory wave patterns that cannot be effectively damped by the dissipation of these first-order schemes. The purpose of this paper is to understand the formation and behavior of these downstream patterns. Our study shows that the downstream errors are generated by the unsteady nature of the viscous shock profiles and behave diffusively. The scenario is as follows. When solving the compressible Euler equations by shock capturing methods, the smeared density profile introduces a momentum spike at the shock location if the shock moves slowly. Downstream waves will necessarily emerge in order to balance the momentum mass carried by the spike for the momentum conservation. Although each family of waves decays in l^∞ and l^2 while they preserve the same mass, the perturbing nature of the viscous or spike profile is a constant source for the generation of new downstream waves, causing spurious solutions for *all* time. Higher order TVD or ENO type interpolations accentuate this problem.

1. INTRODUCTION

In the past two decades there have been tremendous progress in the development of numerical methods for solving the equations governing the unsteady flow of an inviscid, adiabatic ideal gas—the Euler equations. First-order methods usually do not generate numerical oscillations but give poor resolutions due to excessive numerical smearing. Modern high order shock capturing schemes are high order nonlinear schemes that reduce to lower order only near discontinuities to suppress numerical oscillations (e.g., [26, 28, 6, 9]). For shocks of moderate strength these methods give sharp resolutions without oscillations.

However, there are several circumstances where even first-order schemes (such as the Godunov method [4] and the Roe scheme [22]) may give inferior results [19]. One known example is the computation of slowly moving shocks. Here slowly moving means that the ratio of the shock speed to the maximum wave speed in the domain is much smaller than one. Several references have reported the difficulty of computing slowly moving shocks [28, 21, 19], where first-order Godunov or Roe type methods produce spurious long wave oscillations behind the shock, which eventually ruin the downstream solution.

In [28] Colella and Woodward discussed this kind of error in some detail and give a heuristic explanation of it. They also presented additional numerical dissipation terms in their PPM method to damp it. Roberts [21] showed that their explanation of the error is incomplete and that different schemes (i.e., different numerical flux formulas) have significant different levels of these oscillations. This error is inherent to nonlinear systems of equations. The use of total variation diminishing (TVD) concepts in the construction of higher order schemes accentuates the problem. Several improvements on the Roe solver have been suggested [21, 11, 2], which could reduce the level of, but did not completely eliminate, this kind of noise.

Unless a full understanding of the nature of this numerical phenomenon is gained one cannot expect the development of a robust mechanism to completely filter out this kind of oscillations. The goal of this paper is to carefully study this peculiar numerical phenomenon and to understand its formation and propagation. Our study shows that these downstream oscillations propagate along each characteristic family and decay in l^∞ and l^2 while preserving the mass in l^1 norm. They are generated by the unsteadiness of the discrete shock profile. The scenario is as follows. Since all shock capturing methods introduce artificial viscosity in the continuity equation, the smeared shock profile of the density will introduce a momentum spike when the shock is stationary or moves slowly. To maintain momentum conservation, the downstream error will necessarily emerge in order to balance the mass carried by the momentum spike. Although each family of the downstream waves

[1] Email address: jin@math.gatech.edu. Research was supported in part by NSF Grant No. DMS-9404157.

[2] Email address: jliu@math.temple.edu. Research was supported in part by NSF Grant No. DMS-9505275.

0021-9991/96 $18.00

decays in time, our numerical experiments show that the numerical viscous shock or spike profiles are highly *unsteady*. The unsteady nature of the viscous or spike profile becomes a constant source for the generation of new downstream waves, and as a result, the downstream solution is polluted for all time.

In our numerical experiments we also observed the periodic structure of the unsteady viscous shock profile. The period is essentially the time for the shock to propagate one spatial grid.

The importance of such a study goes beyond the slow shock problem. In [21] this kind of error has been blamed for the slow convergence of upwind methods to steady state in transonic flow computations reported, for example, in [15, 29]. Indeed when the solution is near the steady state the shock moves slowly. This will be further explored in Section 5. The study of the unsteadiness of the discrete shock profile is also an active area of research in the aeronautical gas turbine industry because of the need to predict the onset of flutter, as well as the magnitude of forced response loading and oscillations [5, 12].

The outline of the paper follows. In Section 2 we present some numerical results on a Riemann problem of the compressible Euler equations that admits slow shocks. Numerical spikes and downstream oscillations are generated in this example. These results also show that methods using the Lax–Friedrichs scheme as a building block outperform those using the Roe scheme as a building block. In Section 3 a traveling wave analysis on the viscous isentropic Euler equations (Euler equations with viscosity terms in both the continuity and momentum equations) is presented, which shows the existence of the momentum spikes and its difference from the momentum profile of the Navier–Stokes equations. In Section 4 we discuss the downstream waves that balance the momentum spike for the momentum conservation. Numerically we demonstrate that the downstream waves propagate along characteristics and behave diffusively. We also show numerically that the viscous (or spike) profile in these examples highly fluctuate, thus become a constant source for the generation of new downstream waves that ruin the downstream solution for all time. In Section 5 we study the effect of the momentum spike to the computation of steady state solutions and connect it to the non-convergence of high order schemes. We finally make some concluding remarks in Section 6.

For numerical experiments we use a Lax–Friedrichs type scheme (abbreviated as LxF), the second-order relaxation scheme (with van Leer's slope limiter [26]) of Jin and Xin [9] (abbreviated as RELAX2), and the essentially non-oscillatory schemes (both the ENO-ROEs that use the Roe scheme as the building block and the ENO-LLFs that use the Lax–Friedrichs scheme locally as the building block) developed by Shu and Osher [23]. The purpose for the choice of these schemes is that they have quite different viscosity matrices due to different building blocks and interpolation procedures; thus they are excellent examples to illustrate our idea. We would like to point out that similar numerical phenomena occur in essentially all other shock-capturing methods.

In subsequent sections we let $x_{j+1/2}$ be the grid points, $U_{j+1/2}$ be the pointwise value of U at $x = x_{j+1/2}$, and U_j be either the cell average value on the jth cell defined by

$$U_j = \frac{1}{\Delta x}\int_{x_{j-1/2}}^{x_{j+1/2}} U(x,t)\,dx,$$

as in most shock capturing methods, or simply the value of U at the cell center $x_j = (x_{j+1/2} + x_{j-1/2})$ (as in the ENO schemes of Shu and Osher).

2. NUMERICAL SOLUTIONS OF A SLOWLY MOVING SHOCK

Consider the 1D compressible Euler equations of gas dynamics,

$$\begin{aligned} \partial_t \rho + \partial_x m &= 0,\\ \partial_t m + \partial_x(\rho u^2 + p) &= 0,\\ \partial_t E + \partial_x(u(E+p)) &= 0. \end{aligned} \tag{2.1}$$

Here ρ, u, $m = \rho u$, p, and E are respectively the density, velocity, momentum, pressure, and total energy. For a polytropic gas, the equation of state is given by

$$p = (\gamma - 1)(E - \tfrac{1}{2}\rho u^2). \tag{2.2}$$

Let A denote the Jacobian matrix $\partial F(U)/\partial U$. The Euler equations (2.1)–(2.2) are hyperbolic with eigenvalues

$$a^1 = u - c, \quad a^2 = u, \quad a^3 = u + c, \tag{2.3}$$

where $c = \sqrt{\gamma p/\rho}$ is the local speed of sound. The right eigenvectors of A form the matrix $R = (R^1, R^2, R^3)$ given by

$$R = \begin{pmatrix} 1 & 1 & 1\\ u-c & u & u+c\\ H - uc & \frac{1}{2}u^2 & H + uc \end{pmatrix}, \tag{2.4}$$

with $H = c^2/(\gamma - 1) + u^2/2$. The inverse of R defines the left eigenvectors $(L^1, L^2, L^3) = R^{-1}$ of A by

$$R^{-1} = \begin{pmatrix} \frac{1}{2}\left(b_1 + \frac{u}{c}\right) & \frac{1}{2}\left(-b_2 u - \frac{1}{c}\right) & \frac{1}{2}b_2 \\ 1 - b_1 & b_2 u & -b_2 \\ \frac{1}{2}\left(b_1 - \frac{u}{c}\right) & \frac{1}{2}\left(-b_2 u + \frac{1}{c}\right) & \frac{1}{2}b_2 \end{pmatrix}, \quad (2.5)$$

with

$$b_2 = \frac{\gamma - 1}{c^2}, \quad b_1 = b_2 \frac{u^2}{2}. \quad (2.6)$$

Let $U = (\rho, m, E)^{\mathrm{T}}$ be the vector of conserved quantity, $\hat{A}_{j+1/2}$ be the Roe matrix satisfying [22]

$$F(U_{j+1}) - F(U_j) = \hat{A}_{j+1/2}(U_{j+1} - U_j). \quad (2.7)$$

By projecting $U_{j+1} - U_j$ onto $\{R_{j+1/2}\}$ one obtains the characteristic decomposition

$$U_{j+1} - U_j = \sum_{p=1}^{3} \alpha^p_{j+1/2} R^p_{j+1/2}. \quad (2.8)$$

In this decomposition the local characteristic variables $\alpha^p_{j+1/2}$ can be obtained using Roe's average which perfectly resolves stationary discontinuities.

Among our first-order schemes we use the ENO1-Roe and ENO1-LLF by Shu and Osher and a Lax–Friedrichs type scheme. The ENO1-Roe has the numerical flux defined by

$$F_{j+1/2} = \tfrac{1}{2}(F(U_j) + F(U_{j+1})) - \tfrac{1}{2}\mathrm{sgn}(\lambda^p_{j+1/2})(\gamma^p_{j+1} - \gamma^p_j) R^p_{j+1/2}, \quad (2.9a)$$

where γ^p_j is the component of $F(U_j)$ in the pth characteristic family,

$$F(U_j) = \sum_{p=1}^{3} \gamma^p_j R^p_j. \quad (2.9b)$$

The nth order ENO extension of this scheme will be referred to as the ENOn-Roe [23]. These schemes use the Roe scheme as the building block. The ENO1-LLF has the numerical flux defined by

$$F_{j+1/2} = \tfrac{1}{2}(F(U_j) + F(U_{j+1})) - \tfrac{1}{2} a^p_{j+1/2} \alpha^p_{j+1/2} R^p_{j+1/2}, \quad (2.10)$$

where $a^p_{j+1/2} = \max(|\lambda^p_j|, |\lambda^p_{j+1}|)$. The nth order ENO extension of this scheme will be referred to as the ENOn-LLF [23]. These schemes use the Lax–Friedrichs scheme locally as the building block. A Lax–Friedrichs type scheme that we use is

$$F_{j+1/2} = \tfrac{1}{2}(F(U_j) + F(U_{j+1})) - \tfrac{1}{2} a (U_{j+1} - U_j), \quad (2.11)$$

where $a = \sup_U \{|u - c|, |u|, |u + c|\}$.

In addition we also use the RELAX2 in our computations. This idea was originally introduced by Jin and Xin [9]. By introducing a new vector variable $V \in \mathbf{R}^3$, one can couple U and V by the following second-order hyperbolic system

$$\begin{aligned} \partial_t U + \partial_x V &= 0, \\ \partial_t V + A \partial_x U &= -\frac{1}{\varepsilon}(V - F(U)). \end{aligned} \quad (2.12)$$

In (2.12), ε is a small positive parameter called the relaxation time,

$$A = \mathrm{diag}(a_1^2, a_2^2, a_3^2) \quad (2.13)$$

for $a_1 > 0$, $a_2 > 0$, $a_3 > 0$ is a positive diagonal constant matrix satisfying

$$A \geq \frac{\partial F(U)^2}{\partial U}. \quad (2.14)$$

As $\varepsilon \to 0$ (2.12) formally approximates (2.1) via the Chapman–Enskog expansion. By applying the MUSCL scheme [26] to the linear convection in (2.12), coupled with a second-order stiff time integrator, one can obtain a second-order TVD type scheme based on (2.12) that may avoid the Riemann solver or the use of the Roe matrix. In our experiment we choose $\varepsilon = 10^{-6}$ and $a_i = \sup_U |a^i|$.

Except the LxF (2.11), all other schemes that we use here have non-linear viscosities. The RELAX2 and ENO2s are TVD schemes.

We carried out the following 1D test on a Riemann problem of the Euler equation (2.1)–(2.2).

EXAMPLE 2.1. We take the following initial data [19] that gives a Mach-3 shock moving to the right with a speed $s = 0.1096$:

$$\begin{aligned} U_{\mathrm{L}} &= \begin{pmatrix} 3.86 \\ -3.1266 \\ 27.0913 \end{pmatrix} \quad \text{if } 0 \leq x < 0.5; \\ U_{\mathrm{R}} &= \begin{pmatrix} 1 \\ -3.44 \\ 8.4168 \end{pmatrix} \quad \text{if } 0.5 \leq x \leq 1. \end{aligned} \quad (2.15)$$

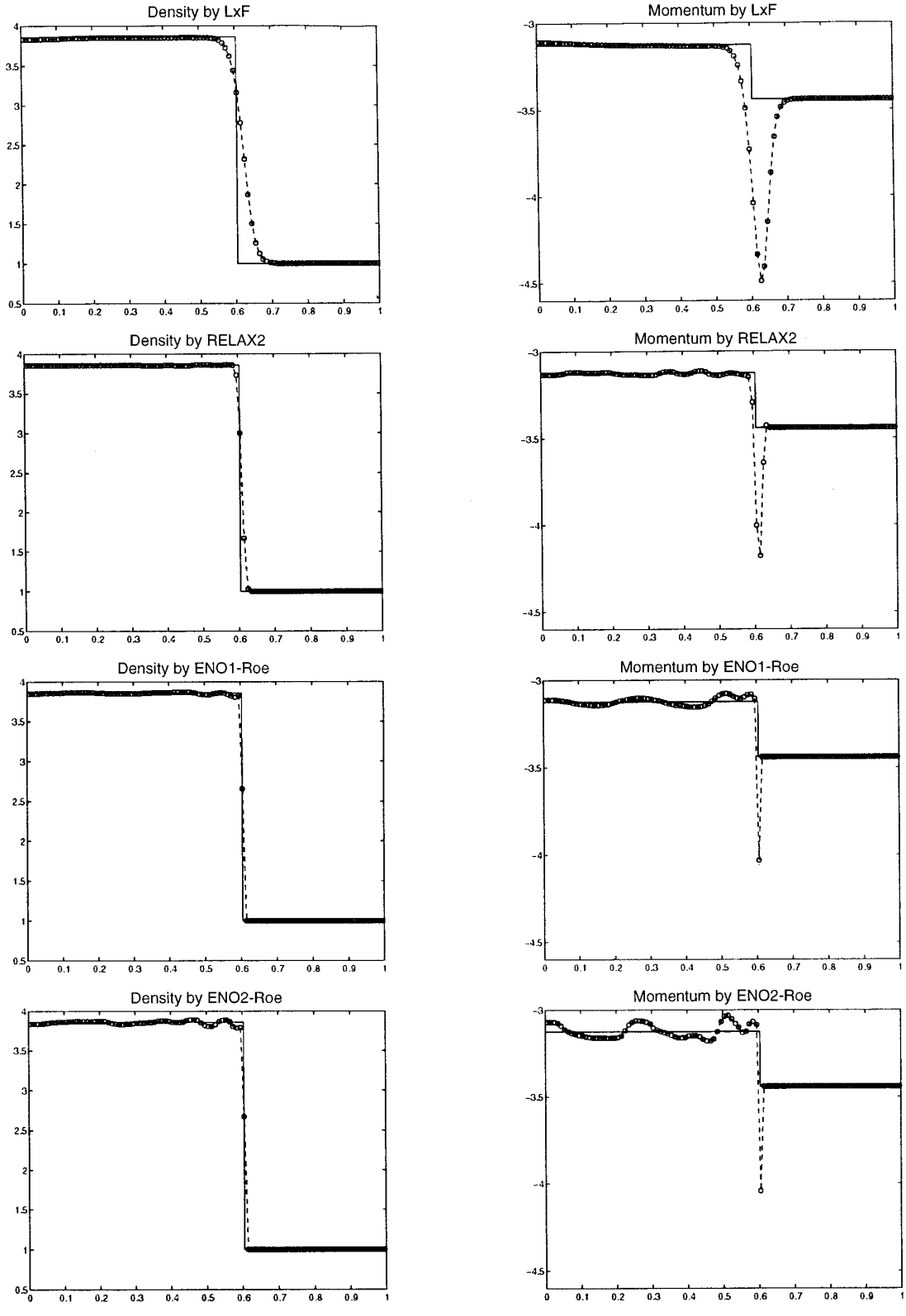

FIG. 2.1. A slowly moving shock computed by LxF, RELAX2, ENO1-Roe, and ENO2-Roe (from top to bottom). In all plots $\Delta x = 0.01$, $\Delta t = 0.001$, $t = 1$. Solid lines are the exact solutions, while the dashed circles are numerical solutions.

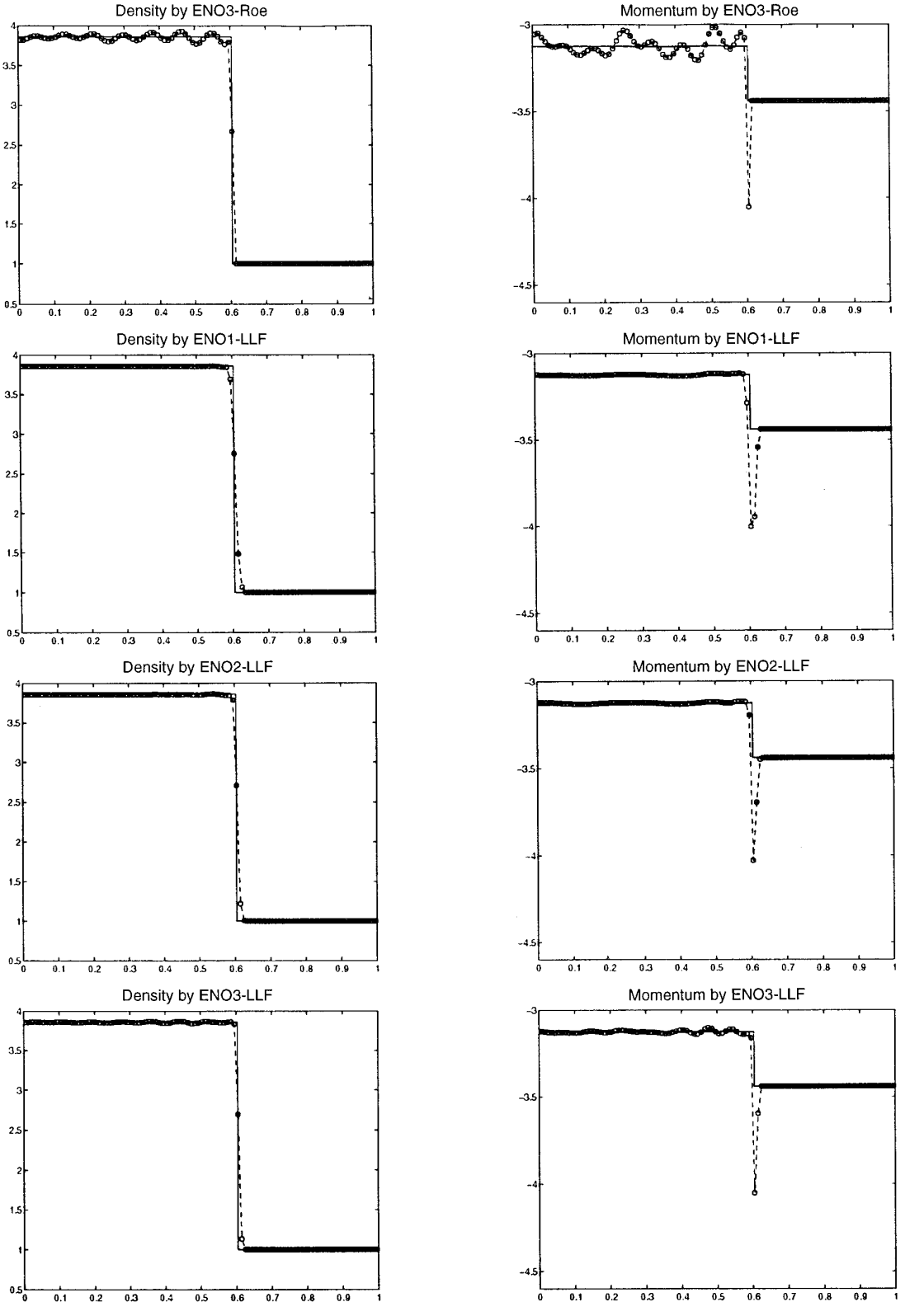

FIG. 2.1 *Continued.* A slowly moving shock computed by ENO3-Roe, ENO1-LLF, ENO2-LLF, and ENO3-LLF (from top to bottom). In all plots $\Delta x = 0.01$, $\Delta t = 0.001$, $t = 1$. Solid lines are the exact solutions, while the dashed circles are numerical solutions.

We take $\gamma = 1.4$ and output the results at $t = 0.95$ in Fig. 2.1. All computations are carried out in the domain [0, 1] with $\Delta x = 0.01$, $\Delta t = 0.001$. All schemes exhibit some level of momentum spikes and postshock oscillations, with the oscillation of LxF almost negligible. The higher order Lax–Friedrichs type schemes produce less severe downstream oscillations than their Roe counterparts. Also higher order interpolations produce more severe oscillations than their lower order counterparts. Overall speaking, the ENO2-LLF gives the best result, followed by RELAX2.

3. THE MOMENTUM SPIKES

3.1. *The Existence of the Spike*

Earlier the momentum (or velocity in Lagrangian coordinates) spikes in stationary shocks were reported in [24] for a mixed type problem and in [27] for the nozzle flow computation. Here we present a traveling wave analysis on the viscous Euler equations, which shows precisely the formation of the momentum spike. Consider the following viscous isentropic Euler equations for density ρ and momentum m:

$$\partial_t \rho + \partial_x m = \varepsilon\, \partial_{xx} \rho, \tag{3.1a}$$

$$\partial_t m + \partial_x \left(\frac{m^2}{\rho} + p(\rho) \right) = \varepsilon\, \partial_{xx} m. \tag{3.1b}$$

Here the pressure $p(\rho) = k\rho^\gamma$ for some constants k and γ. This hyperbolic system has two distinct eigenvalues $u \pm c$, where $u = m/\rho$ is the velocity, $c = \sqrt{\gamma k \rho^{\gamma-1}}$ is the sound speed. Although the true numerical viscosity is far more complicated than those appeared on the right-hand side of Eq. (3.1), a study on (3.1) is sufficient for a full understanding of the numerical momentum spike.

We look at the traveling wave solution to (3.1). Let $\xi = (x - st)/\varepsilon$, where s is the shock speed. Then the traveling wave solution takes the form

$$\rho(x, t) = \phi(\xi), \quad m(x, t) = \psi(\xi) \tag{3.2}$$

with asymptotic states

$$\phi(\pm\infty) = \phi_\pm, \quad \psi(\pm\infty) = \psi_\pm. \tag{3.3}$$

The Rankine–Hugoniot jump condition requires

$$\begin{aligned} &-s(\phi_+ - \phi_-) + (\psi_+ - \psi_-) = 0, \\ &-s(\psi_+ - \psi_-) + \left(\frac{\psi_+^2}{\phi_+} + p(\phi_+) - \frac{\psi_-^2}{\phi_-} - p(\phi_-) \right) = 0. \end{aligned} \tag{3.4}$$

We first assume that the shock is stationary ($s = 0$) and corresponds to the eigenvalue $u - c$. Then the jump condition (3.4) reduces to

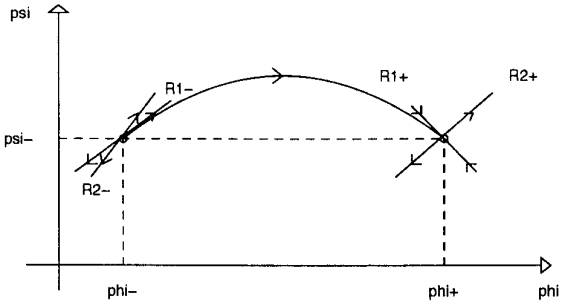

FIG. 3.1. A sketch of the phase portrait of Eqs. (3.7).

$$\psi_+ = \psi_-, \quad \frac{\psi_+^2}{\phi_+} + p(\phi_+) = \frac{\psi^2}{\phi_-} + p(\phi_-), \tag{3.5}$$

and the Lax entropy condition gives

$$0 < u_- - c_- < u_- + c_-, \quad u_+ - c_+ < 0 < u_+ + c_+, \tag{3.6}$$

where $u_\pm = \psi_\pm/\phi_\pm$ and $c = \sqrt{k\gamma\phi^{\gamma-1}}$.

Applying the traveling wave solution (3.2) in (3.1) one gets the following ODEs:

$$\partial_\xi \phi = \psi - \psi_-, \tag{3.7a}$$

$$\partial_\xi \psi = \frac{\psi^2}{\phi} + p(\phi) - \frac{\psi_-^2}{\phi_-} - p(\phi_-). \tag{3.7b}$$

This system has two rest points: $V_+ = (\phi_+, \psi_-)$ on the right and $V_- = (\phi_-, \psi_-)$ on the left on the phase plane of (ϕ, ψ). It has two distinct eigenvalues $\lambda_1 = u - c$ and $\lambda_2 = u + c$, with corresponding eigenvectors $R_1 = (1, u - c)^{\mathrm{T}}$ and $R_2 = (1, u + c)^{\mathrm{T}}$. By the entropy condition (3.6), V_+ is a saddle point with a stable manifold on R_1, and V_- is a source. Thus a heteroclinic orbit **O** will connect V_- and V_+ in the direction of R_1 [25], as shown in Fig. 3.1. (In Fig. 3.1, $R_1^\pm$ and $R_2^\pm$ are the two eigenvectors at $V_\pm$, respectively). Since **O** is smooth and $\partial_\xi \phi$ is not identically zero if $\phi_- \neq \phi_+$, thus (3.7a) implies that ψ is not a constant. Moreover, *whenever $\phi(\xi)$ connects ϕ_- and ϕ_+ with a monotone profile, $\partial_\xi \phi$ becomes a spike.* Thus $\psi = \partial_\xi \phi + \psi_-$ is a spike.

Here we give an example of a stationary shock for the Euler equations (2.1).

EXAMPLE 3.1. We take the initial data

$$U_{\mathrm{L}} = \begin{pmatrix} 2/3 \\ 1/\sqrt{2} \\ 9/14 \end{pmatrix} \quad \text{if } 0 \le x < 0.5;$$

$$U_{\mathrm{R}} = \begin{pmatrix} 2 \\ 1/\sqrt{2} \\ 23/14 \end{pmatrix} \quad \text{if } 0.5 \le x \le 3. \tag{3.8}$$

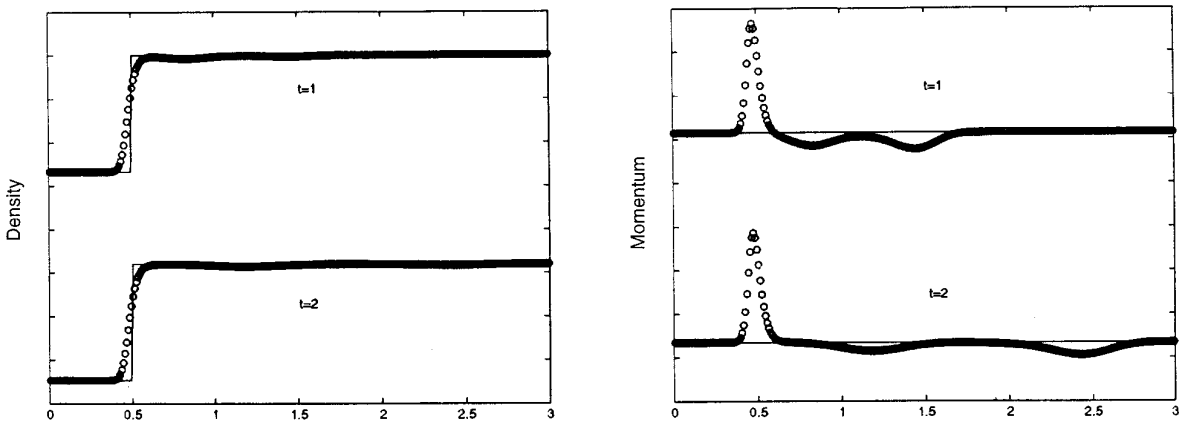

FIG. 3.2. Numerical density ρ and momentum m profiles of Example 3.1 by the LxF. $\Delta x = 0.01$, CFL number = 0.95. Here the solid lines are the exact solution, the circles are numerical solutions.

For this problem the exact solution is exactly the same as the initial data, i.e., a stationary shock, corresponding to the eigenvalue $u - c$, that connects the two initial constant states of the density, while the momentum is the initial constant in the entire domain. We use the LxF to solve this problem. In Fig. 3.2 we depict the numerical results at $t = 1$ and $t = 2$ with 300 points ($\Delta x = 0.01$), CFL number = 0.95. Only density and momentum will be depicted. Other quantities, such as velocity, total energy, pressure, and temperature behave qualitatively similar to the density, thus they will not be depicted here. Observe that the density is smeared out at the shock location $x = 0.5$, and the momentum has an $O(1)$ spike there. Also observable is the two waves that travel to the right, spread out and decaying. These waves will be carefully studied in Section 4. The behavior of the spike differs significantly from the downstream waves, since the spike does not spread out and decay. Note that the shock location is slightly off center of the correct location. This is because a small amount of mass has been carried away by the downstream waves.

In Fig. 3.3 we display the results at $t = 5$ with 100, 200, and 400 points, respectively. As the spatial grid is refined the momentum spike becomes narrower, but the magnitude remains essentially unchanged. The downstream waves observed in Fig. 3.2 have moved to the right, and no new downstream waves have been generated.

Note that the momentum spikes we observed here are solely numerical artifacts. By solving the Riemann problem (3.8) exactly one obtains a monotone momentum.

For this problem, any method using the Roe scheme as the building block [16] (such as the ENO-Roe) does not give such a momentum spike, since the Roe scheme gives the exact stationary shock (no smearing) by its design. However, it is no longer the case when the shock is moving, as shown in Example 2.1.

For a non-stationary shock, the traveling wave solution (3.2) applied to (3.1a) gives

$$\partial_\xi \phi = -s(\phi - \phi_-) + \psi - \psi_-,$$

or

$$\psi = s\phi + \partial_\xi \phi + (\psi_- - s\phi_-). \tag{3.9}$$

Hence *ψ is a superposition of a monotone profile $s\phi$ with a spike corresponding to $\partial_\xi \phi$. When s is small* (*for stationary or slowly moving shock*), *the monotone profile $s\phi$ becomes small and the spike term $\partial_\xi \phi$ dominates. Thus the shock profile of ψ is a non-monotone spike.* Therefore the spike is usually generated in a stationary or slowly moving shock, as shown in our earlier examples. For a strong shock the monotone profile $s\phi$ dominates so the shock profile of the momentum is monotone.

3.2. *The Viscous Profile of the Navier–Stokes Equations*

Since the more physical viscous shock profile is determined by that of the Navier–Stokes equations, we now study the viscous profile of the isentropic Navier–Stokes equations and compare with that of the viscous Euler equations (3.1). The isentropic Navier–Stokes equations are

$$\begin{aligned} &\partial_t \rho + \partial_x m = 0, \\ &\partial_t m + \partial_x \left(\frac{m^2}{\rho} + p(\rho) \right) = \varepsilon\, \partial_{xx} \left(\frac{m}{\rho} \right). \end{aligned} \tag{3.10}$$

Applying the traveling wave solution (3.2) in (3.10), again

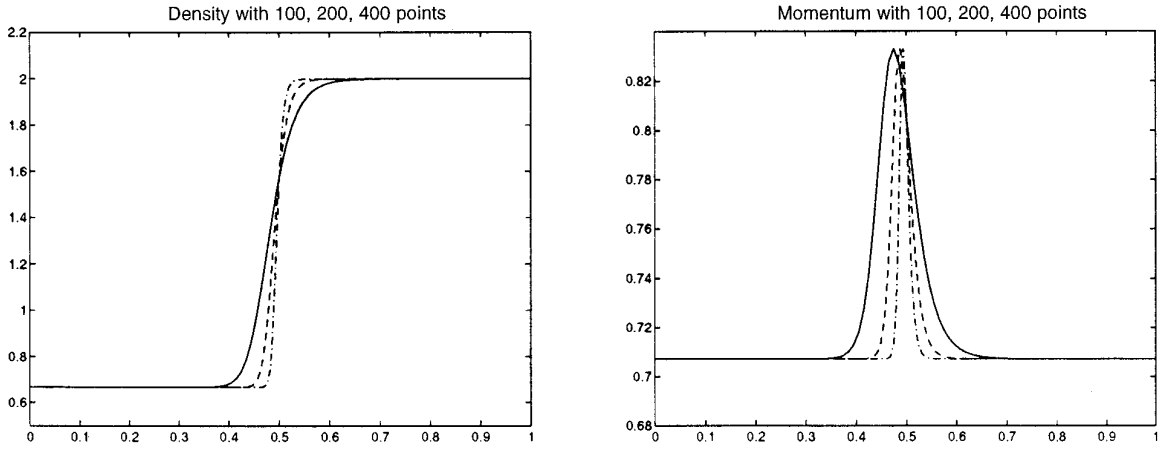

FIG. 3.3. Numerical density ρ and momentum m profiles of Example 3.1 by the LxF with three different mesh sizes. Solid lines: 100 points; dashed lines: 200 points; "———": 400 lines. In all runs CFL number = 0.95.

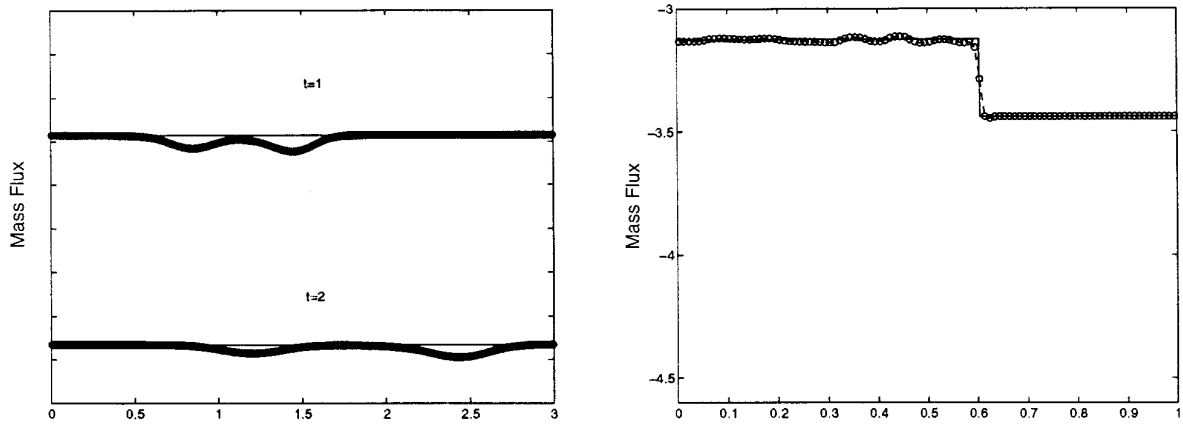

FIG. 3.4. Numerical mass fluxes of Example 3.1 by the LxF (left); numerical mass flux of Example 2.1 by the RELAX2 (right). In both cases the momentum spikes do not appear, but the downstream patterns remain basically unchanged.

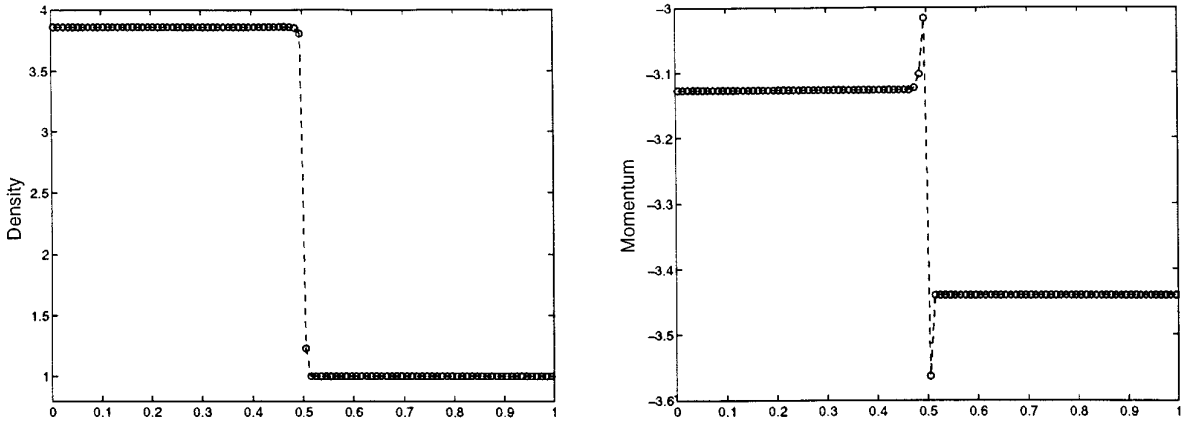

FIG. 4.1. The formation of the spike and downstream wave in the ENO1-Roe calculation of Example 2.1 after five time steps. As the density is smeared, the momentum forms a spike and a downstream wave to balance the mass of the spike for momentum conservation.

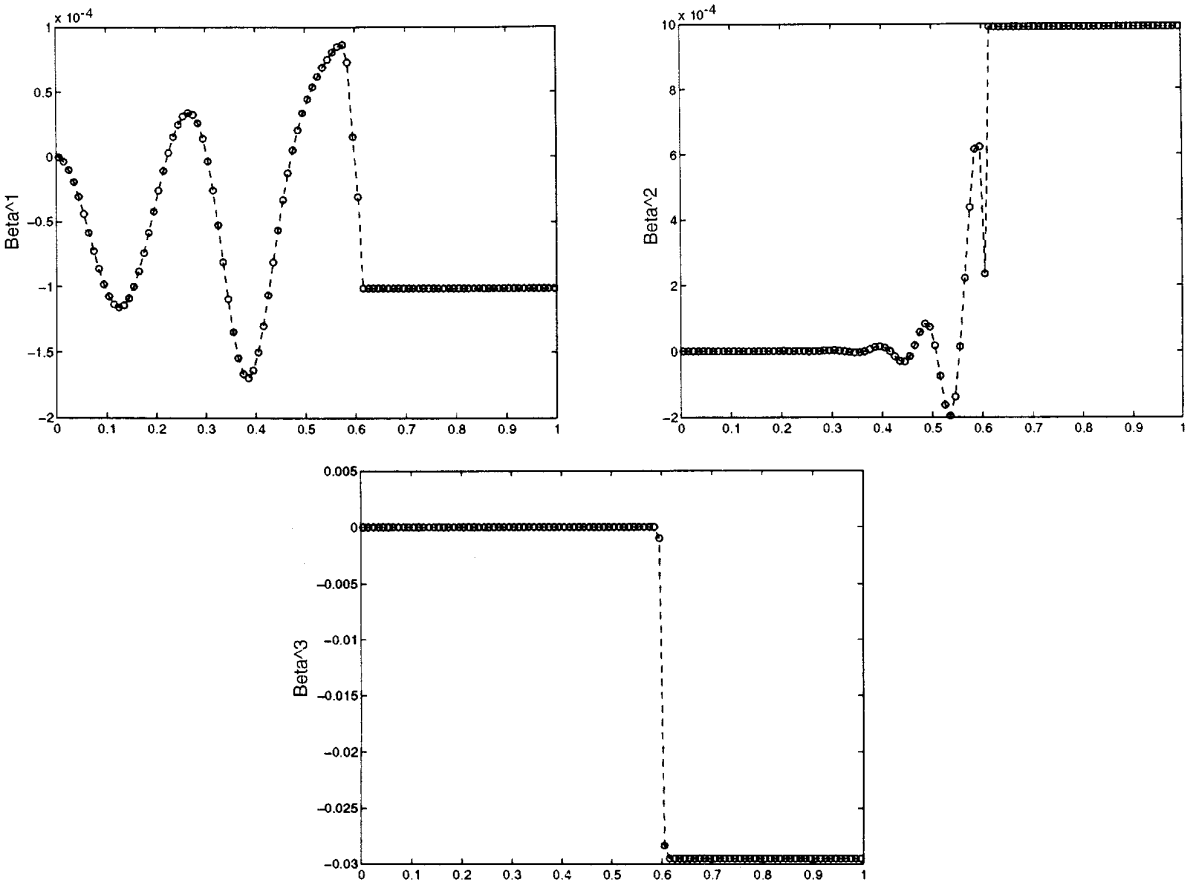

FIG. 4.2. The downstream waves in "characteristic" variables. Note that each wave belongs only to one characteristic family.

assuming the shock speed $s = 0$, one obtains the following ODEs:

$$\psi \equiv \psi_-, \tag{3.11a}$$

$$\partial_\xi \left(\frac{\psi}{\phi}\right) = \frac{\psi^2}{\phi} + p(\phi) - \frac{\psi_-^2}{\phi_-} - p(\phi_-). \tag{3.11b}$$

Equation (3.11a) shows that ψ is a constant, thus it *contains no spike.* Let $f(\phi) = \psi_-^2/\phi + p(\phi)$, then (3.11b) becomes

$$\partial_\xi \left(\frac{\psi}{\phi}\right) = f(\phi) - f(\phi_-). \tag{3.12}$$

Since $f(\phi)$ is a strict convex function and $f(\phi_-) = f(\phi_+)$; hence $f(\phi) - f(\phi_-)$ is always negative between ϕ_- and ϕ_+, so $\partial_\xi(1/\phi)$ does not change sign by (3.12). This implies the monotonicity of $1/\phi$, or ϕ.

When $s \neq 0$, applying the traveling wave solution (3.2) in (3.10a) gives

$$\psi = s\phi + (\psi_- - s\phi_-);$$

thus whenever ϕ is monotone so is ψ. This excludes the possibility of a momentum spike for a moving viscous shock in the Navier–Stokes equations.

In conclusion, even if the viscous profile of ϕ of the Navier–Stokes equations (3.10) could be similar to that of the viscous Euler equations (3.1), the profiles of ψ may be significantly different. Since the physically relevant solution of the Euler equations is considered to be the zero viscosity limit of the Navier–Stokes equations, the momentum spike appeared in the viscous Euler equations is totally unphysical.

Remark 3.1. Although we only present the study on the isentropic Euler and Navier–Stokes equations, the above analysis can be carried exactly through to the full Euler and Navier–Stokes equations. In fact, the argument on the monotonicity of the momentum uses only the continuity equation, which is the same for both the isentropic and the full Euler or Navier–Stokes equations.

Remark 3.2. The non-monotonicity of the momentum profile does not contradict the mathematical stability theory of discrete shocks. It was proved in [13] that the Lax–

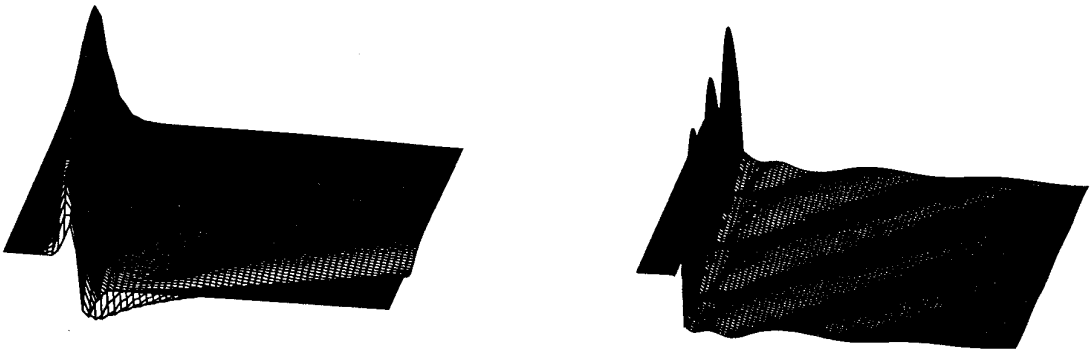

FIG. 4.3. Time evolution of the momentum spike and downstream waves by LxF (top, $t \in [0, 2]$) and ENO1-Roe (bottom, $t \in [0.5, 0.8]$). For better visualization these graphs are displayed upside down. Note the fluctuation of the spike in LxF is much smaller than that of ENO1-Roe. This is also reflected in the downstream wave patterns, the diffusive nature of which is apparent.

Friedrichs scheme applied to general system of conservation laws yields strictly monotone principal eigenvalues at the discrete shock profile. However, as shown here, the primitive variables, such as the momentum, may not be monotone.

Remark 3.3. A related numerical artifact, also induced by numerical viscosity, occurs in the simulation of a strong shock reflecting from a rigid wall [18, 17]. This phenomenon will be further studied in a forthcoming paper.

Remark 3.4. Pressure spike near a contact discontinuity can also be generated by numerical viscosity. This phenomenon was first pointed out by von Neumann and Richtmyer [20] using the Lagrangian formulation of the fluid equations. Similar traveling wave analysis can also be applied to the viscous Euler equations to show this phenomenon. A non-conservative approach was introduced by Karni in [10] to overcome this kind of pressure spike and the consequent noises when computing the multifluid flows.

3.3. *Analytic Elimination of the Spike*

In this section we show an asymptotic connection between the viscous Euler equations and the Navier–Stokes equations, which provides a guidance for a postprocess step that can eliminate the momentum spike. Let

$$\overline{\rho} = \rho, \quad \overline{m} = m - \varepsilon \partial_x \rho \tag{3.13}$$

and apply it to the viscous Euler equations (3.1), one gets (after ignoring the $O(\varepsilon^2)$ term)

$$\begin{aligned} &\partial_t \overline{\rho} + \partial_x \overline{m} = 0, \\ &\partial_t \overline{m} + \partial_x \left(\frac{\overline{m}^2}{\overline{\rho}} + p(\overline{\rho}) \right) = 2\varepsilon \partial_x (\overline{\rho} \partial_x \overline{u}). \end{aligned} \tag{3.14}$$

where $\overline{u} = \overline{m}/\overline{\rho}$. Now the only difference between (3.14) and the Navier–Stokes equations (3.10) is that ε is replaced by $2\varepsilon\rho$. A similar traveling wave analysis carried out in the preceding section can now be applied to (3.14) to show that $\overline{m}$ is monotone; thus it does not have the spike.

Such a transformation has previously been used by Slemrod [24] in his study of mixed hyperbolic–elliptic equations. Note that the difference between m and $\overline{m}$ is negligible in smooth regions. Near the discontinuities $\partial_x \rho$ is big and this transformation changes the momentum dramatically. It is exactly this transformation that cancels out the momentum spike at discontinuities.

3.4. *A Numerical Postprocess that Eliminates the Momentum Spikes*

The modified equation analysis to the shock-capturing methods show that the effect of numerical viscosity is similar to the viscous regularization of the Euler equations. In other words, a shock-capturing method is effectively a higher order approximation to the modified Euler equations (3.1), with a probably different (usually nonlinear) viscosity terms which are method specific. Although our analysis in the proceding sections is for linear viscosities (which is the case for linear schemes such as the LxF), it does provide a good understanding even to nonlinear schemes. Moreover, it provides the guidance on how to remove the momentum spike for general shock capturing methods: *an analog of the transformation* (3.13) *should be performed numerically.* This part of the work is motivated by earlier numerical studies on mixed hyperbolic–elliptic system [1, 8].

A semi-discrete conservative discretization of the Euler equations (2.1) is

$$\partial_t U_j + \frac{1}{\Delta x} (F_{j+1/2} - F_{j-1/2}) = 0. \tag{3.16}$$

The numerical flux for most shock-capturing methods can be written as

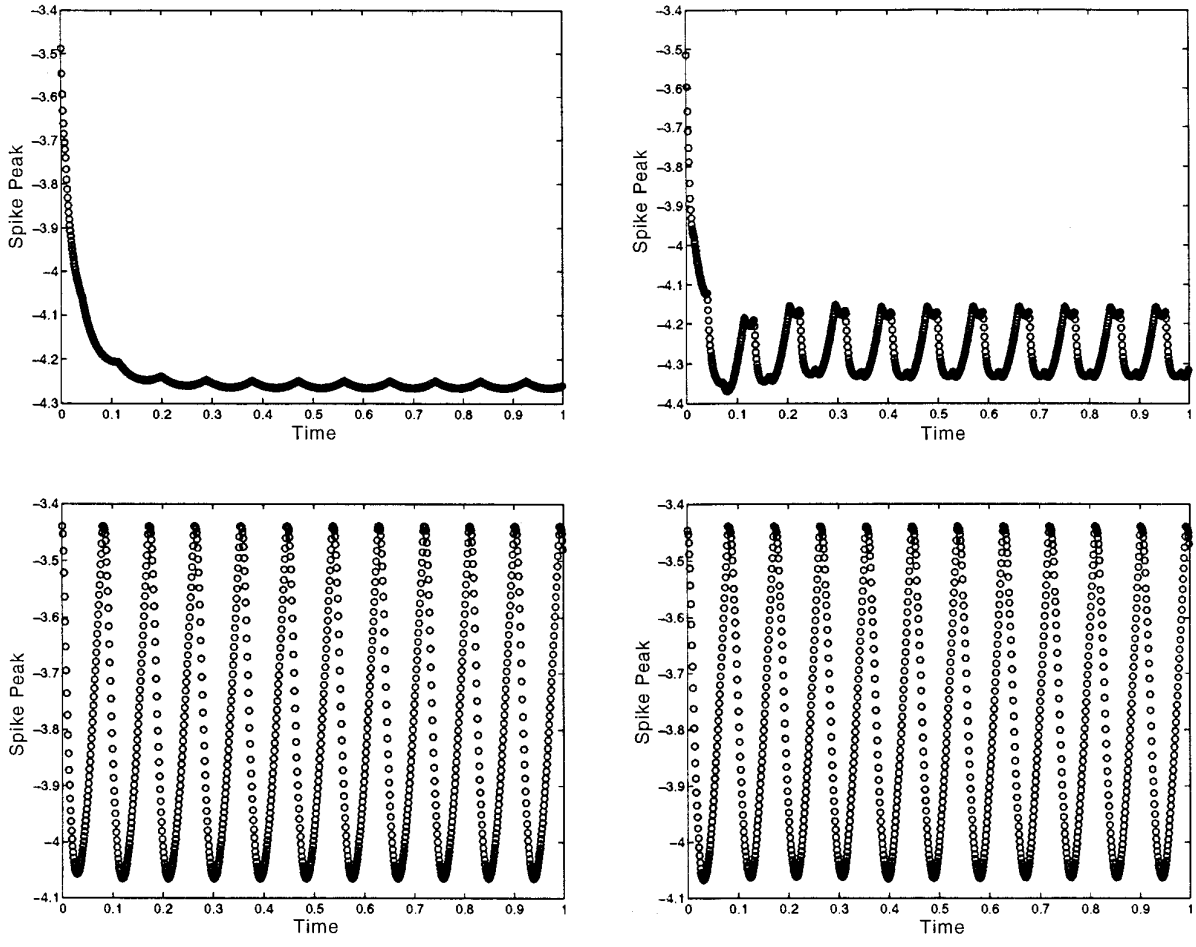

FIG. 4.4. Time evolution of the peak of the momentum spike by (left to right, then top to bottom) LxF, RELAX2, ENO1-Roe, and ENO3-Roe.

$$F_{j+1/2} = \tfrac{1}{2}(F_j + F_{j+1}) - Q_{j+1/2}\,\Delta_{j+1/2}U, \tag{3.17}$$

where $\Delta_{j+1/2}U = U_{j+1} - U_j$, and $Q = Q(U; j)$ is a general numerical viscosity matrix. Applying (3.17) in (3.16) one gets

$$\begin{aligned}\partial_t U_j + \frac{1}{2\Delta x}(F_{j+1} - F_{j-1}) \\ = \frac{1}{\Delta x}(Q_{j+1/2}\,\Delta_{j+1/2}U - Q_{j-1/2}\,\Delta_{j-1/2}U).\end{aligned} \tag{3.18}$$

This system is a discrete analog of the viscous Euler equations (3.1), but now the viscosity term on the right-hand side of (3.18) may be different from those appeared in (3.1). In order to eliminate the numerical spike one has to do a discrete analogy of (3.13). Note that (3.18) is a second order discretization to the following viscous Euler equations

$$\partial_t U + \partial_x F(U) = \partial_x(Q(U)\partial_x U). \tag{3.19}$$

A similar transformation to (3.13) for (3.19) is then

$$\overline{\rho} = \rho, \quad \overline{E} = E, \quad \overline{m} = m - (Q(U)\partial_x U)\cdot e_1, \tag{3.20}$$

where $e_1 = (1, 0, 0)^{\mathrm{T}}$. In order to eliminate the momentum spike generated by the scheme (3.18), we use the discrete analog of (3.20):

$$\overline{m}_j = \tfrac{1}{2}(m_j + m_{j+1}) - (Q_{j+1/2}\,\Delta_{j+1/2})\cdot e_1. \tag{3.21}$$

This is a consistent, second-order discretization of (3.20). By comparing (3.21) with (3.17) we find that

$$\overline{m}_j = m_{j+1/2}. \tag{3.22}$$

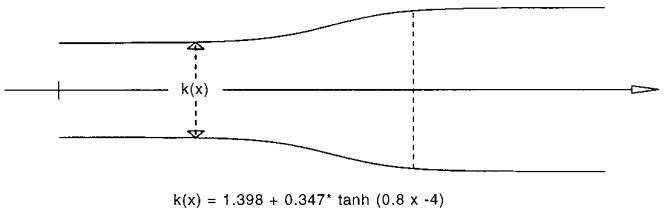

FIG. 5.1. The divergent nozzle.

Thus the discrete transformation (3.21) simply transfers m_j (the cell average value or the value at cell center) into the mass flux $m_{j+1/2}$!

This defines our postprocess step for the momentum spikes. While the momentum m_j has (and will always have) a spike, the mass flux $m_{j+1/2}$ does not have the spike!

Earlier similar transformations were used for mixed hyperbolic–elliptic systems in [1, 8]. This kind of transformation was applied in order to obtain the so-called viscosity–capillarity solutions and to eliminate the velocity spike across the phase boundary.

Remark 3.5. Although the ENO fluxes cannot be written in the general form (3.17), the same postprocess (3.22) works equally well for the ENO, as shown later by our numerical examples.

Remark 3.6. In many numerical computations for hyperbolic systems, even TVD or ENO schemes may generate numerical overshoots or undershoots near a discontinuity. This is hardly surprising since TVD and ENO are concepts for scalar equations or linear systems. They are usually extended to nonlinear systems via the local characteristics decompositions, which is basically an idea for linear systems, as in nonlinear systems there is no global characteristic variables. The numerical spike studied here also looks like an overshoot or undershoot. However, they have distinct features. The overshoots or undershoots can be damped by introducing more numerical viscosities, while more numerical viscosity will make the spike worse. Our study provides an easy method to distinguish the over/undershoots from the spike, since the transformation (3.22) can remove the spike but not the over/undershoots!

Remark 3.7. Since $m_{j+1/2}$ is not a conserved variable, the transformation (3.22) can only be done in the postprocess step. Thus it is basically a cosmetic fix and does not improve the numerical results such as the downstream oscillations.

Remark 3.8. We believe that the study on the momentum spike is also theoretically interesting. It indicates that one cannot obtain a uniform l^∞ convergence on the zero viscosity limit of the viscous Euler equations. Such an estimate could be obtained only after the subtraction of the spike profile.

In Fig. 3.4 we display the mass flux $m_{j+1/2}$ for Example 2.1 (Fig. 3.2) and Example 3.1 (the mass flux of RELAX2). They do not have the spike, but they have essentially the same features as the momentum m_j elsewhere.

4. THE DOWNSTREAM OSCILLATIONS

We bear in mind that all reasonable shock-capturing methods are in conservative form. Due to the conservation of momentum, the total mass of momentum carried by the spike profile should be compensated by an equal amount of momentum mass elsewhere. This explains the initial formation of the downstream waves. In this section we will also numerically demonstrate that each downstream wave travels along with a characteristic family, and its magnitude (or l^∞ and l^2 norms) decays in time but the mass (or l^1 norm) conserves. Moreover, we will show the unsteadiness of the discrete shock for slowly moving shocks, which contributes to the downstream oscillations for all time.

In Fig. 4.1 we output the result of ENO1-Roe for Example 2.1 after five time steps to illustrate the formation of the spike and a downstream wave. As the density is smeared, the momentum forms a spike and a downstream wave. The spike and the downstream wave carry the same mass so the total momentum is conserved.

In order to demonstrate that the downstream are diffusive and propagate along the characteristics, we use the Roe decomposition (2.8), where α^p represents the component of $U_{j+1} - U_j$ in the pth characteristic family. We define the numerical "characteristic" variable as

$$\beta_j^p = \sum_{i \le j} \alpha_{i+1/2}^p \, \Delta x. \tag{4.1}$$

A distinction between the dispersive oscillations and the downstream oscillations studied here is that the latter lie only in its own characteristic family. For example, a wave appears in β^p does not appear in β^q for $p \neq q$. These can be seen in Fig. 4.2. We also see that each wave moves away with the corresponding characteristic speed and behaves diffusively (spread out and decayed).

If the shock is stationary, then the viscous or the spike profile will become stationary as well, after the initial formation of the spike and the downstream waves, as shown in Fig. 3.2. However, when the shock moves (slowly), the viscous or spike profile cannot be steady. In Fig. 4.3 we display the time evolution of the momentum profile of the LxF and ENO1-Roe for Example 2.1. After some time the fluctuation in the spike of LxF becomes quite small, thus it generates new downstream waves which are almost negligible. For ENO1-Roe, however, the spike (viscous) profile keeps fluctuating in and $O(1)$ manner, and new and strong downstream waves are produced for all time. The diffusive nature of the downstream waves are evident in both pictures.

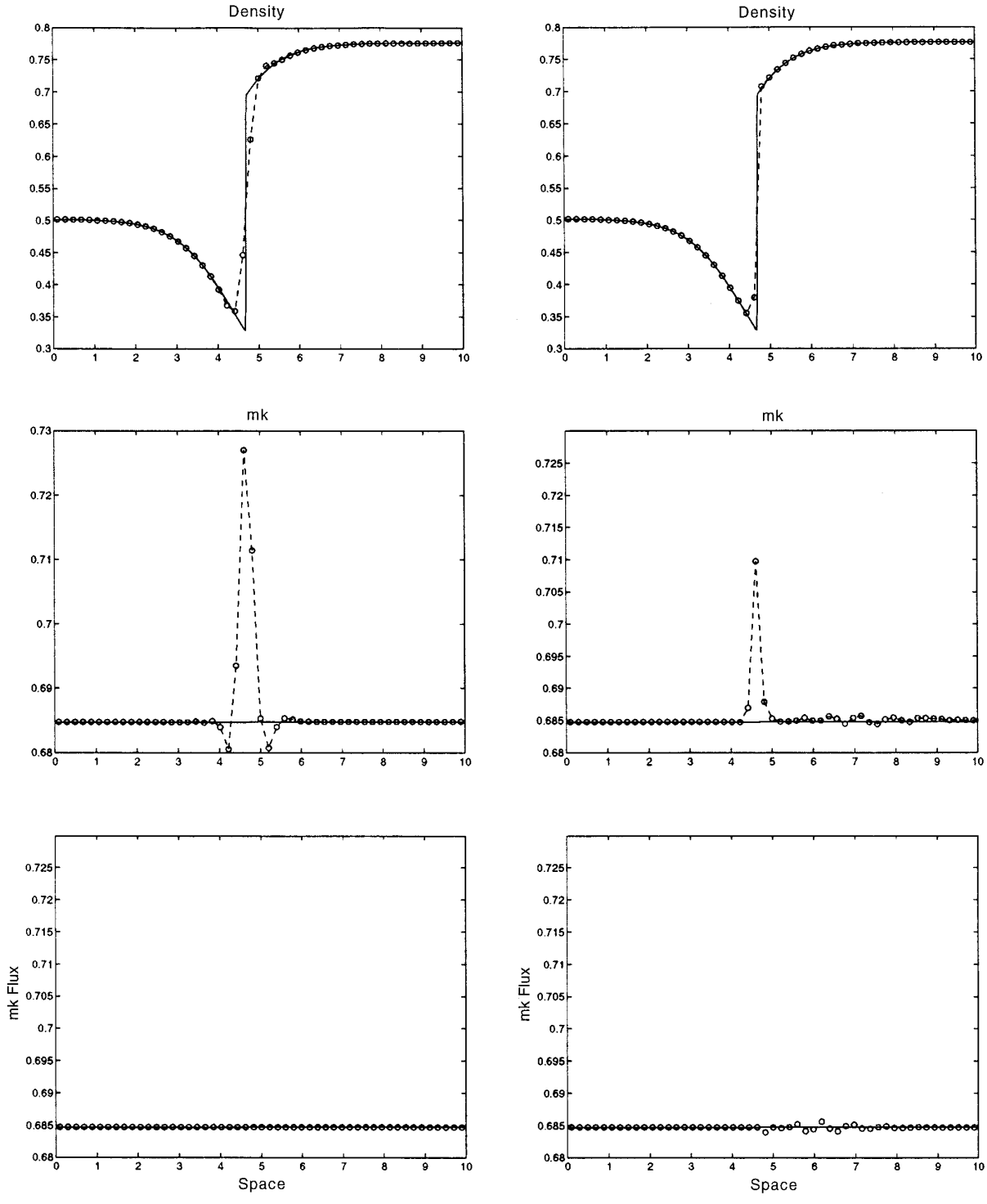

FIG. 5.2. Numerical solutions of the divergent nozzle flow problem (5.1)–(5.3) at $t = 672.40$ with 51 points and $\Delta t = 0.046$ by the RELAX2 (left) and ENO3 (right). Here the solid lines are the exact solution; the dashed circles are numerical solutions.

In Fig. 4.4 for the same example we plot the peak of the momentum spikes for some schemes as a function of time. The oscillatory nature of the spike is evident with varying magnitude of fluctuations. This figure shows that the upwind type schemes (ENO-Roe) have viscous profiles more unsteady than those of the LxF and RELAX2. We would like to point out that it is the amount of mass change (instead of the change of the magnitude of the spike) during the perturbation of the viscous profile that determines the level of the downstream errors, due to the conservation

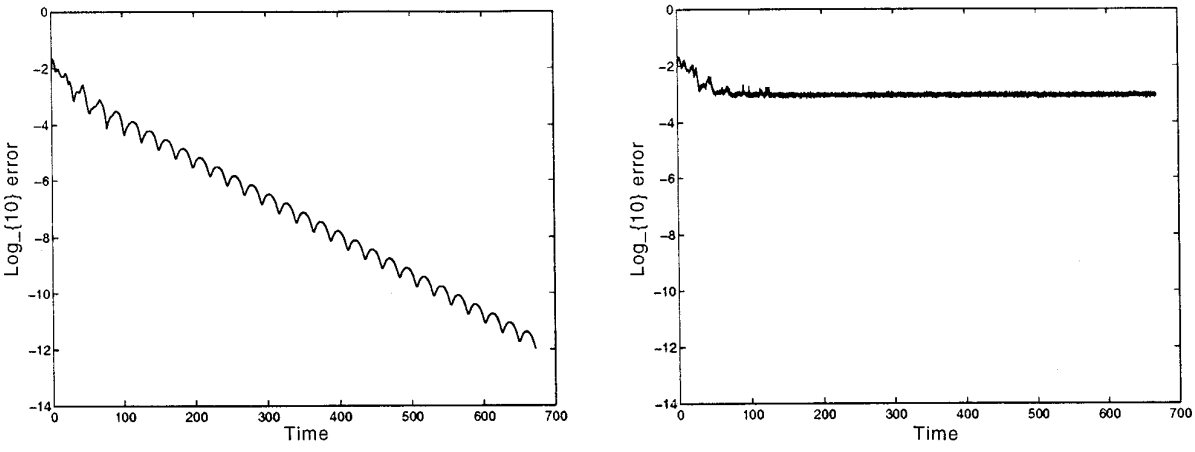

FIG. 5.3. The convergence study of the RELAX2 (left) and the ENO3-Roe (right).

of the momentum. *The more the mass of the spike profile varies the more strongly the downstream waves emerge for momentum conservation.* Interesting is that *the peaks are essentially periodic, with the duration of each period agrees with the time for the shock to move one grid point.*

Remark 4.1. Recall that the definition of a discrete traveling wave solution Φ_j^n, an approximation of $U(x_j, t_n)$, $t_n = n\ \Delta t$, requires

$$\Phi_j^{nq} = \Phi_{j-np}^0, \tag{4.2}$$

where $s\ \Delta t/\Delta x = p/q$ for some relative prime integers p and q. The stability of such discrete shock for the Lax–Friedrichs scheme was established by Jennings [7] for scalar equations and by Majda and Ralston [16] and J.-G. Liu and Xin [13] for nonlinear systems. The periodicity of the momentum peaks in Fig. 4.4 shows the stability of the discrete traveling wave solution Φ_j^n for these schemes modulus the time for the shock to travel one grid point. This is because, when $s\ \Delta t \ll \Delta x$, there exists a sufficiently large q such that $|q(s\ \Delta t) - \Delta x| < s\ \Delta t$, or $|s\ \Delta t/\Delta x - 1/q| \leq 2/q^2$. However, within each period the shock profile is unsteady, which becoming the source of the new downstream waves in all time for these schemes.

A scheme that completely eliminates such an error should have a steady discrete viscous profile. However, this is impossible if the shock is moving (slowly), since it takes many time steps for the shock to move to the next cell, and in between the viscous profile has to perturb in order to keep the unsteady nature of the solution. An alternative is to have a scheme that has a more steady viscous profile, and our numerical experiment shows that the Lax–Friedrichs scheme could serve such a purpose. Thus the idea is to smear out the shock by a Lax–Friedrichs type scheme. This is clearly against the high resolution principle. What we would like to emphasize here is that when one develops a shock capturing scheme, one should not only concentrate on

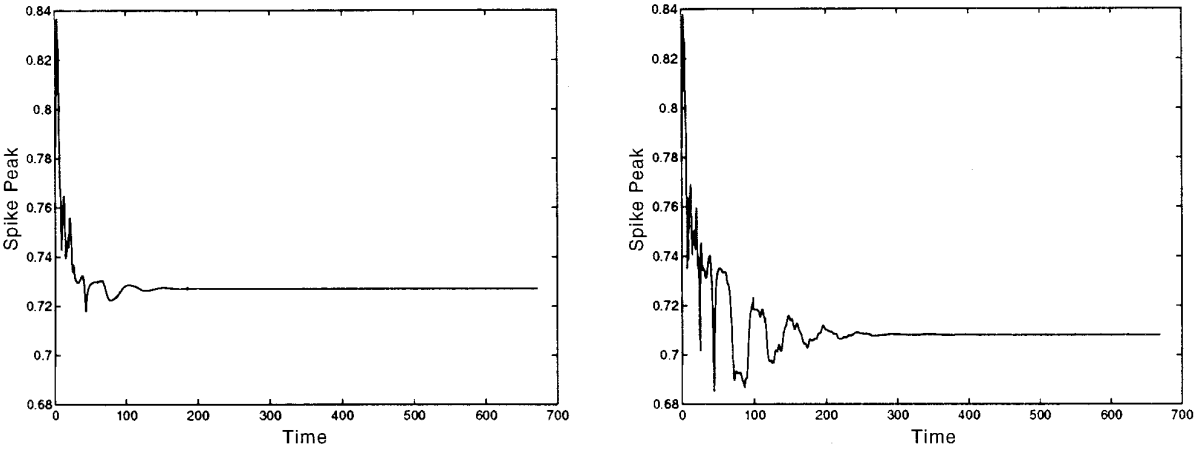

FIG. 5.4. The peak of the momentum spike for the RELAX2 (left) and ENO3-Roe (right).

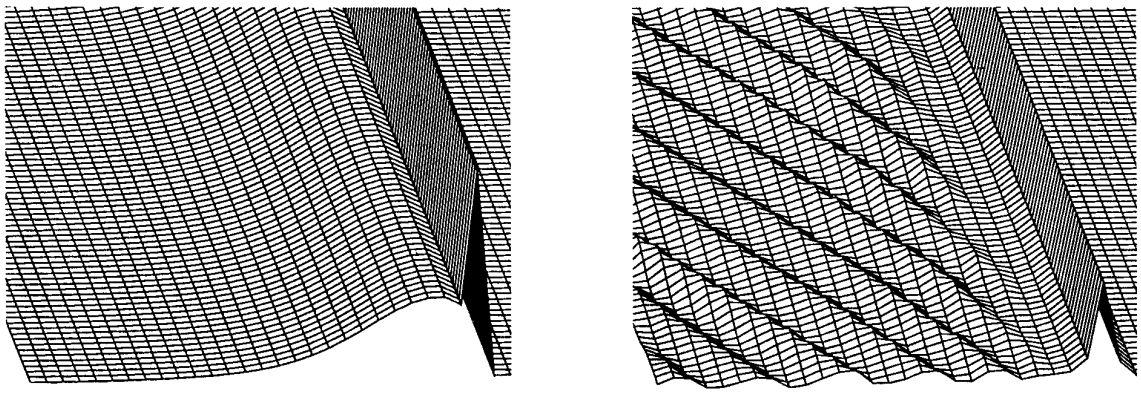

FIG. 5.5. Time evolution of the numerical solutions by ENO1-Roe (left) and ENO3-Roe (right) for $t \in [500, 504.6]$. The x-axis reads from left to right.

the resolution (by counting the number of points across a shock), but also pay special attention to the stability of the numerical viscosity. A scheme that has both high resolution and a more stable viscosity is ideal. According to this standard, the ENO-LLFs are better than ENO-Roes, since the former offers essentially the same resolution but have more stable viscosities.

The discrete shock profile perturbs even when the shock does not move slowly. Thus the downstream oscillations exist even for fast shocks. However, in the fast shock case the momentum profile is monotone, thus does not leave much room for the shock profile to perturb. In other words, each perturbation does not change the mass of the viscous profile much, and the downstream errors become negligible. For slow shock the momentum profile has a spike, which increases the mass of the viscous profile and the relative mass change in each perturbation, so the downstream errors become more significant. This also illustrates why the downstream errors in the density is far less significant. Since the density is monotone, thus the relative change in the mass of the viscous profile is smaller than that of the momentum.

In summary, although each family of the downstream waves decays time-asymptotically, the perturbing spike or viscous profile is a constant source for the generation of new downstream waves, causing the downstream oscillation for *all* time. Higher order methods use higher order interpolations, which amplify the level of oscillations and exhibit rich but spurious postshock structures.

5. STEADY STATE CALCULATIONS

A closely related problem is the steady state calculation. In this section we show numerically how the momentum spike contributes to the non-convergence to the steady state solution of some high resolution shock capturing schemes. Indeed when the solution is near the steady state the shock moves slowly and the numerical errors discussed earlier will occur is such a circumstance. Here, we use the quasi-one-dimensional nozzle flow as an example to illustrate this phenomenon.

The quasi-one-dimensional nozzle flow can be described by the following Euler equations with a geometric source term

$$\begin{aligned} \partial_t(\rho k) + \partial_x(mk) &= 0, \\ \partial_t(mk) + \partial_x(\rho u^2 k + pk) &= p\partial_x k, \\ \partial_t(E\mathrm{k}) + \partial_x(u(E+p)k) &= 0, \end{aligned} \tag{5.1}$$

where $k(x)$ is area of the nozzle. We consider only a divergent nozzle from [3] with

$$k(x) = 1.398 + 0.347 \tanh(0.8x - 4). \tag{5.2}$$

as shown in Fig. 5.1. The steady flow conditions were supersonic inflow, subsonic outflow with a shock. In all the calculations the computational domain is $0 \le x \le 10$. The numerical initial conditions are obtained using linear interpolation between the exact steady state boundary values, and the boundary conditions are specified on the three conservative variables ρk, mk, Ek, one the left boundary $x = 0$ and ρk on the right boundary $x = 10$, as

$$\begin{aligned} (\rho k)(0,t) &= 0.5277, \quad (mk)(0,t) = 0.6855, \\ (ek)(0,t) &= 1.4465, \quad (ek)(10,t) = 3.454. \end{aligned} \tag{5.3}$$

For the given data (5.3) there is a stationary shock near $x = 4.816$. We also use zeroth-order space extrapolation to obtain the numerical boundary conditions for the unknown variables mk, Ek at the outflow boundary $x = 10$ [30].

We use the RELAX2, ENO1-Roe, and ENO3-Roe to compute the above nozzle flow. Previously the slow convergence of high resolution methods have been reported [15, 29]. In Fig. 5.2 we use RELAX2 and ENO3-Roe, with 51 points, $\Delta t = 0.046$, and output the results at $t = 672.40$. Only ρ, mk and the flux of mk will be depicted in Fig. 5.2. The mk profiles in all these schemes exhibit spurious spikes at the shock location. The ENO-Roe3 resolves the steady shock better, with a narrower viscous and spike profile. This is due to the fact that ENO-Roe uses the Roe matrix which is advantageous for stationary discontinuities. However, one can observe the oscillatory behavior of ENO3-Roe in the downstream direction. This causes the problem of non-convergence for ENO3-Roe. We also see that the fluxes of mk do not have the spikes in both methods.

To study the numerical convergence we define the l^2 error function as

$$\text{error} = \sqrt{\begin{array}{c}(\rho k(t+\Delta t) - \rho k(t))^2 + (mk(t+\Delta t) - mk(t))^2 \\ + (Ek(t+\Delta t) - Ek(t))^2\end{array}} \tag{5.4}$$

and plot $\log_{10}$(error) in Fig. 5.3. By the time we stopped $t = 672.40$ the RELAX2 has reached an error of 10^{-10}, while the error for ENO3-Roe stays in the order of 10^{-3}. In Fig. 5.4 we plot the magnitude of the momentum spike and found that they become steady for both RELAX2 (at $t \approx 150$) and ENO3-Roe (at $t \approx 300$). For a steady state solution one does not expect that the study in Section 4 will play any role in understanding the oscillatory behavior of ENO3-Roe shown in Fig. 5.2. Rather the oscillations seem to be caused by high order interpolations near the spike. To justify this we compare the results of ENO1-Roe and ENO3-Roe in Fig. 5.5. Although ENO1-Roe has a bigger spike profile it does not exhibit any downstream oscillations.

It seems that the downstream oscillation in the ENO3-Roe calculation exhibits some periodic structure. Thus a reasonable definition of convergence for this kind of method should be the convergence modulus this period.

6. DISCUSSIONS AND CONCLUSIONS

In this paper we studied the effect of numerical viscosities for slowly moving and steady shocks in Euler equations. We showed that it is the unsteady numerical viscosity that causes the downstream oscillations. When the density profile is smeared by numerical viscosities, the momentum forms a spike due to the artificial viscosity in the continuity equation. The mass carried by this spike is compensated by downstream waves of equal mass for momentum conservation. These downstream waves propagate along characteristics and decay in l^∞ and l^2. A perturbing viscous or spike profile is a constant source for the generation of new downstream waves, which explains the downstream oscillations for all time.

Note the schemes we used in the paper are monotone, TVD, or ENO schemes. All these monotonicity theories are established only for scalar equations, or linear systems. For non-linear systems there are no global characteristic variables; thus these methods are usually extended to non-linear systems using the idea for linear systems, i.e., via the so-called local characteristic decomposition (using the Roe matrix, for example). Since there is no theory for the monotonicity of these methods for non-linear systems, it is not surprising to see the non-monotone behavior represented by the spike and downstream oscillations reported here. It seems to us that, to fully solve this problem, instead of applying scalarly monotone, TVD, or ENO scheme to non-linear systems, one needs a method that is *systematically* "monotone, TVD, or ENO." One also needs to choose numerical viscosity properly so it mimics the physical viscosity of the Navier–Stokes equations. An ideal scheme should have both a high resolution and a more stable numerical viscosity. These require good theories for both inviscid and viscous nonlinear systems [14] and remain open and challenging research subjects for the future.

Upon the completion of this work we were informed of the work [31] on the same subject but using a dynamical system approach.

ACKNOWLEDGMENTS

We appreciate the helpful discussions with Professors Tai-Ping Liu, Stanley Osher, and Zhou-Ping Xin. In addition we thank Professor Antonio Marquina for his comments that helped to improve the presentation of the paper.

REFERENCES

1. B. Cockburn and H. Gau, *SIAM J. Sci. Comput.,* to appear.
2. R. Donat and A. Marquina, *J. Comput. Phys.* **125**(1), 42 (1996).
3. H. M. Glaz and T. P. Liu, *Adv. in Appl. Math.* **5,** 111 (1984).
4. S. K. Godunov, *Mat. Sb.* **47,** 271 (1959).
5. K. C. Hall, W. S. Clark, and C. B. Lorence, *ASME J. Turbomach.* **116,** 477 (1994).
6. A. Harten, B. Engquist, S. Osher, and S. Charkravarthy, *J. Comput. Phys.* **71,** 231 (1987).
7. G. Jennings, *Commun. Pure Appl. Math.* **27,** 25 (1974).
8. S. Jin, *SIAM J. Appl. Math.* **55,** 1536 (1995).
9. S. Jin and Z. P. Xin, *Commun. Pure Appl. Math.* **48,** 235 (1995).
10. S. Karni, *J. Comput. Phys.* **112,** 31 (1994).
11. H.-C. Lin, *J. Comput. Phys.* **117,** 20 (1995).
12. D. R. Lindquist and M. B. Giles, *AIAA J.* **32,** 46 (1994).

13. J.-G. Liu and Z. P. Xin, *Arch. Rat. Mech. Anal.* **125,** 217 (1993).
14. T. P. Liu, *Mem. Am. Math. Soc.* **238** (1985).
15. C. C. Lytton, *J. Comput. Phys.* **73,** 395 (1987).
16. A. Majda and J. Ralston, *Commun. Pure Appl. Math.* **32,** 445 (1979).
17. R. Menikoff, *SIAM J. Sci. Comput.* **15,** 1242 (1994).
18. W. F. Noh, *J. Comput. Phys.* **72,** 78 (1987).
19. J. J. Quirk, *Int. J. Numer. Methods Fluids* **18,** 555 (1994).
20. R. D. Richtmyer and K. W. Morton, *Difference Methods for Initial-Value Problems* (Wiley-Interscience, New York, 1967).
21. T. W. Roberts, *J. Comput. Phys.* **90,** 141 (1990).
22. P. L. Roe, *J. Comput. Phys.* **43,** 357 (1981).
23. C.-W. Shu and S. Osher, *J. Comput. Phys.* **83,** 32 (1989).
24. M. Slemrod and J. E. Flaherty, ''Numerical Integration of a Riemann Problem for a van der Waals Fluid,'' in *Phase Transformations*, edited by C. A. Elias and G. John, 1986.
25. J. Smoller, *Shock Waves and Reaction-Diffusion Equations* (Springer-Verlag, NewYork/Berlin, 1983).
26. B. van Leer, *J. Comput. Phys.* **32,** 101 (1979).
27. M. Wilcoxson and V. Manousiouthakis, *J. Comput. Phys.* **115,** 376 (1994).
28. P. Woodward and P. Colella, *J. Comput. Phys.* **54,** 115 (1984).
29. H. C. Yee, NASA TM-89464, May, 1987 (unpublished).
30. H. C. Yee, R. F. Warming, and A. Harten, *J. Comput. Phys.* **57,** 327 (1985).
31. M. Arora and P. L. Roe, *J. Comput. Phys.,* to appear.